



RESEARCH ARTICLE

10.1029/2024JD042378

Key Points:

- The relationship between the vertically integrated water vapor (IWV) and the downward, thermal-infrared irradiance F_{TIR} is studied
- This study is based on observations of different air masses advected to the Central Arctic during the Arctic winter 2019–2020
- It is observed that the IWV- F_{TIR} relationship is affected by the IWV as well as by the vertical temperature profile of the water vapor

Correspondence to:

C. Seidel,
seidelc@tropos.de

Citation:

Seidel, C., Althausen, D., Ansmann, A., Wendisch, M., Griesche, H., Radenz, M., et al. (2025). Close correlation between vertically integrated tropospheric water vapor and the downward, broadband thermal-infrared irradiance at the ground: Observations in the Central Arctic during MOSAiC. *Journal of Geophysical Research: Atmospheres*, 130, e2024JD042378. <https://doi.org/10.1029/2024JD042378>

Received 2 SEP 2024
Accepted 18 MAR 2025

Author Contributions:

Conceptualization: Clara Seidel, Dietrich Althausen, Albert Ansmann, Manfred Wendisch, Holger Baars, Ronny Engelmann
Data curation: Holger Baars, Ronny Engelmann
Formal analysis: Clara Seidel, Dietrich Althausen, Albert Ansmann, Manfred Wendisch, Andreas Walbröl
Investigation: Clara Seidel, Dietrich Althausen
Methodology: Clara Seidel, Dietrich Althausen, Manfred Wendisch
Resources: Dietrich Althausen, Hannes Griesche, Martin Radenz, Julian Hofer, Sandro Dahlke, Marion Maturilli, Andreas Walbröl, Holger Baars, Ronny Engelmann

© 2025. The Author(s).

This is an open access article under the terms of the [Creative Commons Attribution License](https://creativecommons.org/licenses/by/4.0/), which permits use, distribution and reproduction in any medium, provided the original work is properly cited.

Close Correlation Between Vertically Integrated Tropospheric Water Vapor and the Downward, Broadband Thermal-Infrared Irradiance at the Ground: Observations in the Central Arctic During MOSAiC

Clara Seidel¹ , Dietrich Althausen¹ , Albert Ansmann¹ , Manfred Wendisch² , Hannes Griesche¹ , Martin Radenz¹ , Julian Hofer¹ , Sandro Dahlke³ , Marion Maturilli³ , Andreas Walbröl⁴ , Holger Baars¹ , and Ronny Engelmann¹ 

¹Leibniz Institute for Tropospheric Research, Leipzig, Germany, ²Leipzig Institute for Meteorology, Leipzig University, Leipzig, Germany, ³Helmholtz Centre for Polar and Marine Research, Alfred Wegener Institute, Potsdam, Germany, ⁴Institute for Geophysics and Meteorology, University of Cologne, Cologne, Germany

Abstract The impact of the vertical distribution of tropospheric water vapor on the cloud-free downward, broadband thermal-infrared irradiance (F_{TIR}) was quantified using observations in the Central Arctic, north of 85°N, collected during the Arctic winter. The water vapor profiles were measured with a temporal resolution of 30 s using a Raman lidar. The observations revealed maximum values of integrated water vapor (IWV) contents of 3.6 kg m⁻². Seven measurement cases of several-hour durations of slowly changing air masses were examined. Furthermore, 53 rather short-term (10 min) measurement cases were studied. The temporal evolution of the slowly changing air masses revealed a linear relationship between F_{TIR} and IWV with slopes between 7.17 and 12.95 W kg⁻¹ and a coefficient of determination larger than 0.95 for most of the selected cases. The slopes and the ordinate intercepts showed a dependence on the water vapor-weighted mean temperature (representative temperature of the water vapor distribution). The temperature determined with the Stefan-Boltzmann law from F_{TIR} correlated with the representative temperature with a coefficient of determination of 0.92. The analysis of 53 independent short-term observations of different air masses confirmed the linear relationship between F_{TIR} and IWV at wintertime cloud-free conditions in the Arctic (coefficient of determination of 0.75, slope of 19.95 W kg⁻¹, and ordinate intercept of 107.22 W m⁻²).

Plain Language Summary The temperature rises much faster in the Arctic than in other regions of the world. At a higher temperature, the air can contain more water vapor. Atmospheric rivers carry moist air to the Central Arctic not only at the surface but also at higher altitudes. The vertical distribution of water vapor impacts the downward, broadband thermal-infrared irradiance (F_{TIR}), but the question is how and how much. For the first time, water vapor profile measurements with high temporal and vertical resolution were conducted in the frame of the MOSAiC campaign 2019–2020 during the Central Arctic winter half year. The article investigates these measurements of water vapor profiles together with temperature profiles and F_{TIR} measurements. The results show a close correlation between the water vapor content and the simultaneously measured F_{TIR} . It is observed that the relationship between both quantities can be described by a linear function for the evaluated cloud-free winter data. The results also show that the temperature of the water vapor and hence the vertical distribution of the water vapor plays an essential role for the F_{TIR} .

1. Introduction

Atmospheric water vapor is an important greenhouse gas exceeding the CO₂ greenhouse effect by a factor of at least two (Myhre et al., 2013). In the Arctic, the temperature rises faster than in other regions of the globe (Boeke & Taylor, 2018; Graverson et al., 2008; Screen & Simmonds, 2010; Wendisch et al., 2017, 2023), partly related to feedback mechanisms caused by water vapor. For example, moist air is advected to the Arctic along atmospheric rivers (Nash et al., 2018; Wendisch et al., 2023) at different altitudes into and above the Arctic dome (Bozem et al., 2019; Law et al., 2014). By this, water vapor is advected to high altitudes, leading to changes in the vertical water vapor distribution and the radiation budget of the Arctic.

Radiosondes and lidar systems are used for measurements of vertical water vapor distributions. There are scarce observational stations equipped with radiosondes in the Arctic, but not in the Central Arctic. Lidar systems are not

Supervision: Dietrich Althausen, Albert Ansmann, Manfred Wendisch, Ronny Engelmann

Validation: Clara Seidel, Dietrich Althausen, Albert Ansmann

Visualization: Clara Seidel, Dietrich Althausen

Writing – original draft: Clara Seidel, Dietrich Althausen

Writing – review & editing: Clara Seidel, Dietrich Althausen, Albert Ansmann, Manfred Wendisch, Hannes Griesche, Martin Radenz, Julian Hofer, Sandro Dahlke, Andreas Walbröl, Holger Baars, Ronny Engelmann

routinely used in the Arctic. For that reason, the knowledge about the vertical distribution of water vapor in the Arctic is mainly based on atmospheric models, added by a few research campaigns.

The downward, broadband thermal-infrared irradiance (F_{TIR}) is a key quantity for assessing the radiative impact of atmospheric water vapor on the surface radiative energy budget. The relationship between vertical water vapor profiles and F_{TIR} in the Arctic is less strongly influenced by the low aerosol particle concentrations common in the Arctic regions compared to midlatitudes. Doyle et al. (2011) quantified an average impact of about 19 W m^{-2} in F_{TIR} for a change of 5.2 mm in precipitable water (PW) using measurements in the Arctic during moisture intrusion events in cloud-free conditions. This is equivalent to an impact of 3.7 W m^{-2} for a change of 1 kg m^{-2} in the integrated water vapor (IWV). The evaluation of water vapor measurements from the South Pole region by Town et al. (2005) has revealed that the contribution of the atmospheric water vapor to F_{TIR} at clear skies dominates over the CO_2 impact by a factor two, both in summer and winter.

Clark et al. (2021) investigated the trend in F_{TIR} at the surface from 1984 to 2017 during clear-sky conditions by using ERA-Interim reanalysis data finding a positive trend in F_{TIR} in the Arctic. They concluded that increasing temperatures and water vapor amounts are the reason for 90% of the clear-sky F_{TIR} trend. Ruckstuhl et al. (2007) and Ghatak and Miller (2013) considered the relationship between monthly mean values of IWV and F_{TIR} in the Alps and in the Arctic for all-sky conditions and found a nonlinear correlation. The correlation function shows a much steeper slope for small IWV values, which occur in the Arctic winter, than for higher IWV values during Arctic summer conditions. This correlation implies a large influence on F_{TIR} by temporal changes in the wintertime IWV, for example, due to the advection of water vapor or an increasing moisture content in the context of Arctic warming. Heinemann et al. (2022) used a regional climate model for the period of the Multidisciplinary drifting Observatory for the Study of Arctic Climate (MOSAiC) campaign and found a linear correlation between specific humidity in the lowest 2,000 m of the atmosphere and F_{TIR} for clear-sky conditions during the wintertime. The results from their model studies imply differences in the relationship for clear-sky and all-sky conditions and for different seasons. Pace et al. (2023) used measurements of the IWV and F_{TIR} from Greenland to investigate parameterization formulas linking IWV, screen-level temperature, and F_{TIR} from surface observations. Their results show a dependence of the bias of the parameterization for F_{TIR} on the measured IWV and the screen-level temperatures.

These studies emphasize the influence of the integrated water vapor on F_{TIR} at the surface, but most of the results are based on simulations. Corresponding measurements in the Central Arctic are rare. In particular, height-dependent water vapor and temperature profile measurements would help in the analysis as input for radiative transfer simulations, as has been shown in model studies (e.g., Graversen et al. (2008), Screen and Simmonds (2010) and Barrientos-Velasco et al. (2022)).

During the MOSAiC campaign performed in 2019 and 2020 (Shupe et al., 2022), the German research vessel *Polarstern* (Knust, 2017) was frozen in the Arctic sea ice for 1 year (with few interruptions). Among others, atmospheric water vapor and temperature profiles, and solar and thermal-infrared irradiances at the surface have been collected continuously. Profiles of the water vapor mixing ratio (WVMR) were derived from continuous Raman lidar measurements during polar night. One year of vertically resolved water vapor measurements with a high temporal resolution of 30 s have been collected in the Central Arctic winter, north of 85°N .

The MOSAiC observations have been analyzed to study the relationship between the cloud-free F_{TIR} and the vertically distributed water vapor and temperature to identify the characteristics of the water vapor profile and its impact on F_{TIR} . After an overview of the instruments and the applied methods in Section 2, the background for the selection of the cases in this study is explained in Section 2.6. The observations and results are presented in Section 3. Firstly, one case study is explained in detail (Section 3.1). Then, slow transformations of air masses are investigated at the location of *Polarstern* over several hours for seven measurement cases (Section 3.2). In Section 3.3, randomly selected measurements of different air masses and different days are evaluated to characterize the relationship between the vertically distributed water vapor and F_{TIR} for cloud-free winter cases in the Central Arctic. Section 4 provides the summary and concluding remarks.

2. Instrumentation and Methods

2.1. MOSAiC Expedition

In this study, measurements collected during the MOSAiC expedition (Shupe et al., 2022) are used. This campaign took place from October 2019 until October 2020. The German icebreaker *Polarstern* was frozen in the ice north of Siberia and shifted with the transpolar drift close to the North Pole until it reached the Fram Strait. The Raman lidar PollyXT (Engelmann et al., 2016) was installed in the OCEANET container (Engelmann et al., 2021). The container housed also the microwave radiometer named LHUMPRO-243-340 for Low-HUMidity high-precision PROfiler (henceforth only LHUMPRO). The instrument is described, and its measurements are discussed in detail by Walbröl, Crewell, et al. (2022) and Walbröl, Orlandi, et al. (2022). The radiation measurement part of OCEANET was located close by the container and included a pyrgeometer for the measurements of F_{TIR} (Section 2.3). Radiosondes were launched at the same height as the lidar position regularly four times per day.

2.2. Raman Lidar Observations of Water Vapor Profiles

The Raman lidar PollyXT (Engelmann et al., 2016) is a multiwavelength Raman and polarization lidar, which emits radiation at the three wavelengths λ of 355 nm, 532 nm, and 1064 nm; it uses 12 channels for the detection of the backscattered light. The resolution of the raw data is 30 s temporally and 7.5 m vertically. For the determination of the WVMR profiles, the inelastic backscattering is measured from the molecules of water vapor (at $\lambda_{\text{H}_2\text{O}} = 407$ nm) and nitrogen (at $\lambda_{\text{N}_2} = 387$ nm) (Melfi et al., 1969; Wandinger, 2005; Whiteman, 2003b). Those measurements are only possible during nighttime due to the low Raman backscattering and are limited to cloud-free conditions or to the altitudes below the cloud base.

During the data processing, dead time (Engelmann et al., 2016) and background corrections (Weitkamp, 2006) are applied to the signals. No range correction is needed for the calculation of the WVMR. An overlap correction is omitted, assuming the same overlap for the water vapor and the nitrogen channel (Foth et al., 2015). A vertical smoothing and temporal averaging is applied to both signals centered around each measurement bin.

Two averaging periods and signal-to-noise ratio (SNR) limits are applied during the water vapor retrieval procedure. The vertical smoothing length is set to three bins (≈ 22.5 m) close to the surface and increases with height in dependence of the SNR (Heese et al., 2010) to a maximum smoothing length of 101 bins (≈ 750 m) for all measurements. For the lower altitudes, the temporal smoothing is fixed to 10 min and a minimum $\text{SNR} \geq 5$ is set as the limit for the data quality. This allows the retrieval of water vapor up to several kilometers height. To obtain the water vapor data at higher altitudes with very low water vapor content, it is necessary to average up to 60 min and to reduce the limit of the SNR down to $\text{SNR} \geq 1$. For the evaluation of longer time periods, missing values in upper heights are linearly interpolated by using profiles of the measurements before and after. Then, the low-altitude profiles are completed by the high-altitude profiles. By this, the WVMR profiles are retrieved up to the tropopause (Ohneiser et al., 2021) height.

The height-resolved WVMR $w(z)$ in g kg^{-1} is determined by Foth et al. (2015), Wandinger (2005), and Whiteman (2003b):

$$w(z) = C_{\text{H}_2\text{O}} \cdot \frac{F_{\text{N}_2}[T(z)]}{F_{\text{H}_2\text{O}}[T(z)]} \cdot \frac{P_{\text{H}_2\text{O}}(z)}{P_{\text{N}_2}(z)} \cdot \frac{\exp\left[-\int_0^z \alpha_{\lambda_{\text{N}_2}}\right]}{\exp\left[-\int_0^z \alpha_{\lambda_{\text{H}_2\text{O}}}\right]}, \quad (1)$$

from the signal ratio of the measured backscattered signals from the atmospheric water vapor and nitrogen molecules $P_{\text{H}_2\text{O}}(z)/P_{\text{N}_2}(z)$. The ratio $F_{\text{N}_2}[T(z)]/F_{\text{H}_2\text{O}}[T(z)]$ represents the temperature dependence of the filter transmission (Whiteman, 2003a, 2003b). The last factor of Equation 1 depicts the different atmospheric transmissions at the two used wavelengths λ_{N_2} and $\lambda_{\text{H}_2\text{O}}$ with the atmospheric (particle and molecular) extinction coefficients α_{λ_i} . The calibration constant $C_{\text{H}_2\text{O}}$ is determined using a linear fit between collocated lidar and radiosonde profiles (Foth et al., 2015; Melfi & Whiteman, 1985). The calibrations of 49 selected cloud-free profiles between 22 October 2019 and 29 February 2020 yielded an averaged calibration constant of $15.96 \pm 0.37 \text{ g kg}^{-1}$ (Seidel, 2022).

According to Dai et al. (2018) and Whiteman (2003b), the relative error in the WVMR is expressed by

$$\frac{\sigma_w^2}{w^2}(z) = \frac{\sigma_C^2}{C^2} + \frac{\sigma_{R_F}^2}{R_F^2}(z) + \frac{\sigma_{R_w}^2}{R_w^2}(z) + \frac{\sigma_{\Delta T_r}^2}{\Delta T_r^2}(z), \quad (2)$$

where σ_x expresses the uncertainty of the quantity x . The uncertainties of the computed differential transmission ΔT_r and the temperature dependence of the filter transmission R_F are negligible (Foth et al., 2015). The relative error of the signal ratio R_w results from the statistical error of the measured lidar signals and is calculated from the SNRs of the two signals (Dai et al., 2018).

The integrated water vapor (IWV) I_{lidar} is defined as the integral of the water vapor density $\rho_{\text{H}_2\text{O}}(z)$ from z_{min} to z_{max} . $\rho_{\text{H}_2\text{O}}(z)$ is the product of the water vapor mixing ratio $w\text{H}_2\text{O}$ and the density of dry air ρ_d (Dai et al., 2018; Elgered et al., 1982):

$$I_{\text{lidar}} = \int_{z_{\text{min}}}^{z_{\text{max}}} \rho_{\text{H}_2\text{O}}(z) dz = \int_{z_{\text{min}}}^{z_{\text{max}}} w(z)\rho_d(z) dz. \quad (3)$$

The density of dry air $\rho_d(z)$ is calculated from the radiosonde data of temperature $T(z)$ and pressure $p(z)$. The minimum height z_{min} is set to 30 m for all calculated IWV values to minimize the direct influence of the ship. The maximum height z_{max} is set to the tropopause height of each case (Ohneiser et al., 2021), but can also be the height where the lidar signals show $\text{SNR} < 1$.

The error of the IWV from the lidar is calculated by error propagation:

$$\Delta I_{\text{lidar}} = \sqrt{\sum_z [\rho_d(z) \cdot \sigma_w(z) \cdot \Delta z]^2} \quad (4)$$

with the uncertainty σ_w of the WVMR. No error is considered for the air density calculated from the radiosonde data. Another uncertainty occurs due to possible time differences between the radiosonde launches and the lidar measurements. This uncertainty could not get considered, because the temperature profile changes between two radiosonde launches are not accessible.

2.3. Measurements of Temperature Profiles and Downward, Broadband Thermal-Infrared Irradiance (F_{TIR})

Temperature profiles were measured with radiosondes of the type Vaisala RS41 four times per day during MOSAiC (Maturilli et al., 2021). The relative measurement errors are very small with a maximum of 0.1% in temperature and 4% in relative humidity (Survo et al., 2014). The drift of the radiosonde with the wind is neglected in further discussions, as well as the time, the radiosonde needs for ascending. Both effects play a minor role for the comparisons with the lidar profile due to the temporal smoothing of the lidar data over 10 min.

For this study, the radiosonde data are temporally and vertically linear interpolated on the lidar time and height grid to derive temperature profiles between the soundings. Measurements of F_{TIR} are taken from the “Kipp&Zonen Pyrogeometer CGR4,” which was part of the “Scalable automatic weather station” (SCAWS) that was located close to the lidar during MOSAiC. The instrument delivers continuous F_{TIR} measurements of the hemisphere with a high temporal resolution of a few seconds. The uncertainty of the instrument was 0.41% as determined during extensive ground-based calibrations.

2.4. Temperature From Surface Radiation Measurements

The temperature T_{rad} derived on the basis of the Stefan-Boltzmann law is given by:

$$T_{\text{rad}} = \sqrt[4]{\frac{F_{\text{TIR}}}{\epsilon \cdot \sigma}}, \quad (5)$$

with the measured broadband thermal-infrared irradiance F_{TIR} , the Stefan-Boltzmann constant $\sigma = 5.67 \cdot 10^{-8} \text{ W m}^{-2} \text{ K}^{-1}$, and the emissivity ϵ . Here, we apply a parameterization of the emissivity of the atmosphere suggested by Jin et al. (2006):

$$\epsilon = (0.0003(T - 273.16)^2 - 0.0079(T - 273.16) + 1.2983) \cdot \left(\frac{e}{T}\right)^{1/7}, \quad (6)$$

with the atmospheric temperature T in K and the water vapor pressure e in hPa at the surface. The emissivities derived from Equation 6 reach values between 0.69 and 0.73 for the chosen cases in this study.

2.5. Representative Temperature of the Vertical Water Vapor Profile

To derive a vertically representative temperature T_{rep} for each water vapor profile, a water vapor-weighted mean temperature is calculated from the corresponding radiosonde temperature profile. This temperature is calculated as weighted arithmetic mean as:

$$T_{\text{rep}} = \sum_{i_{z_{\text{min}}}}^{i_{z_{\text{max}}}} G_i \cdot T_{\text{RS},i}, \quad \text{with: } \sum_{i_{z_{\text{min}}}}^{i_{z_{\text{max}}}} G_i = 1, \quad (7)$$

where the weights G_i consider the water vapor density derived from Raman lidar data at the height z corresponding to the height bin i_z . The weights G_i are defined as:

$$G_i = \frac{\rho_{\text{H}_2\text{O},i}}{\sum_i \rho_{\text{H}_2\text{O},i}} = \frac{w_i \rho_{\text{d},i}}{\sum_i w_i \rho_{\text{d},i}}, \quad (8)$$

with the absolute humidity $\rho_{\text{H}_2\text{O},i}$. The profiles of the temperature T_{RS} and the density of dry air ρ_{d} are taken from the radiosonde measurements; the profiles of the WVMR $w_{\text{H}_2\text{O}}$ are derived from the Raman lidar measurements.

Additionally, the representative height of each water vapor profile H_{rep} is defined to assess a height of the vertical water vapor profile that is related to T_{rep} . The height H_{rep} is determined as the height, at which the measured temperature is equal to the determined representative temperature T_{rep} of the water vapor profile. Due to the observed strong surface temperature inversion typical in the Arctic and represented in most of our measurements, often two heights are found that fulfill these conditions. In these cases, the upper height is selected. The height H_{rep} represents the height below which the water vapor has mainly temperatures larger than T_{rep} . Smaller values of H_{rep} depict water vapor profiles having mainly water vapor at larger temperatures than profiles with a higher H_{rep} .

H_{rep} allows also the determination of the water vapor fraction between the surface and the height with T_{rep} . The ratio of the IWV between the ground and the height H_{rep} to the IWV of the total lidar profile is denoted as the near-surface fraction f_{ns} of the IWV. It is defined by

$$f_{\text{ns}} = \frac{\int_{z_{\text{min}}}^{H_{\text{rep}}} \rho_{\text{H}_2\text{O}}(z) \, dz}{\int_{z_{\text{min}}}^{z_{\text{max}}} \rho_{\text{H}_2\text{O}}(z) \, dz} = \frac{\int_{z_{\text{min}}}^{H_{\text{rep}}} w(z) \rho_{\text{d}}(z) \, dz}{\int_{z_{\text{min}}}^{z_{\text{max}}} w(z) \rho_{\text{d}}(z) \, dz}. \quad (9)$$

The near-surface fraction depends on IWV and H_{rep} and hence is not an additional independent quantity of the vertical water vapor profile. f_{ns} tends to be smaller for lower H_{rep} (smaller upper limit of the integral) and tends to be larger for profiles with more water vapor at lower heights (larger terms in the integral). f_{ns} helps to describe the impact of the water vapor on F_{TIR} in more detail at heights below H_{rep} .

2.6. Lidar Data Handling, Quality Check, and Selection of Lidar Observational Periods for the IWV Data Base

The analyses in this study are confined to cloud-free conditions. The Raman lidar data (particle backscattering signal at 1064 nm, Section 2.2) were used to manually select time periods with cloud-free conditions. The lidar was operated continuously with a temporal resolution of 30 s, whereas radiosonde data were only available every

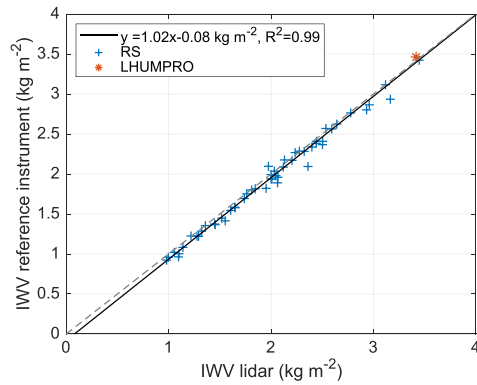


Figure 1. Correlation between the IWV measurements from the lidar and radiosonde (RS) or microwave radiometer (LHUMPRO) for the selected 53 profiles.

6 hr. Temperature profiles between two radiosonde launches were determined by linear interpolation of the radiosonde profiles around. Using the density profile from the radiosonde measurements, an IWV was determined from the lidar measurements (Equation 3).

Figure 1 shows the comparison of the lidar-retrieved IWV values with those derived from measurements with radiosondes and LHUMPRO. The radiosonde-retrieved IWV values were used for the comparison of 52 of the 53 selected cases. In one case, the comparison of the cloud-free lidar profile (15 November 2019 at 9:00–9:10 UTC) was done with the IWV from LHUMPRO, because the radiosonde data could not be used for comparison during this time due to changes in the atmosphere and the only two radiosonde launch times at 04:50:42 UTC and 10:54:00 UTC on this day. The resulting ratios of the lidar-derived IWV values and the radiosonde- or microwave radiometer-derived IWV values are between 94.2% and 113.8% and show a very good correlation with a coefficient of determination of 0.99.

The variations of F_{TIR} as a function of the tropospheric water vapor distribution are investigated in two ways. Firstly, the temporal evolution of the air masses over the location of *Polarstern* is investigated over several hours using seven cloud-free periods (Sections 3.1–3.2.3). These investigations reflect slow air mass transformations and corresponding WVMR and F_{TIR} changes. A combination of sequentially measured profiles is used for these investigations. Secondly, the relations are examined by means of 53 individual measurements at different days (Section 3.3). The temporal distance between the profiles is at least 6 hr, but mainly 1 day and more. Hence, the measurements can be regarded as independent from each other and representing different air masses. All measurements were performed at cloud-free conditions between 27 October 2019 and 29 February 2020. Figure 2 gives an overview over the selected individual WVMR cases, including individual profiles from the seven evaluated longer time periods. Each case consists of one WVMR profile from a measurement, smoothed over at least 10 min in lower altitudes (Section 2.2) and represented by its mean and range of values over all altitudes. The maximum height of each profile is the respective tropopause height. The WVMR values are lower and cover a range between 0 and 1.4 g kg^{-1} . Periods with higher and lower WVMRs alternate depending on the large-scale synoptic conditions with higher WVMR values related to storms (Rinke et al., 2021; Seidel, 2022). Short periods with large WVMR values are observed between October and December 2019 as well as at the end of February, whereas a longer period of very small WVMR values is found during January and February 2020.

3. Observations and Results

3.1. Case Study of 13 November 2019

Particle backscatter profiles indicated cloud-free conditions between 08:00 and 20:00 UTC on 13 November 2019.

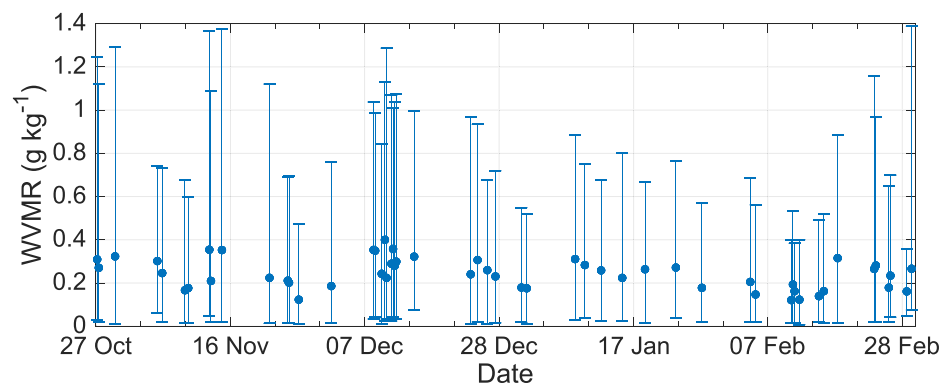


Figure 2. WVMR values of the 53 selected individual cases measured between 27 October 2019 and 29 February 2020. Each WVMR profile is represented by its mean (dot) and the range of values (vertical bar).

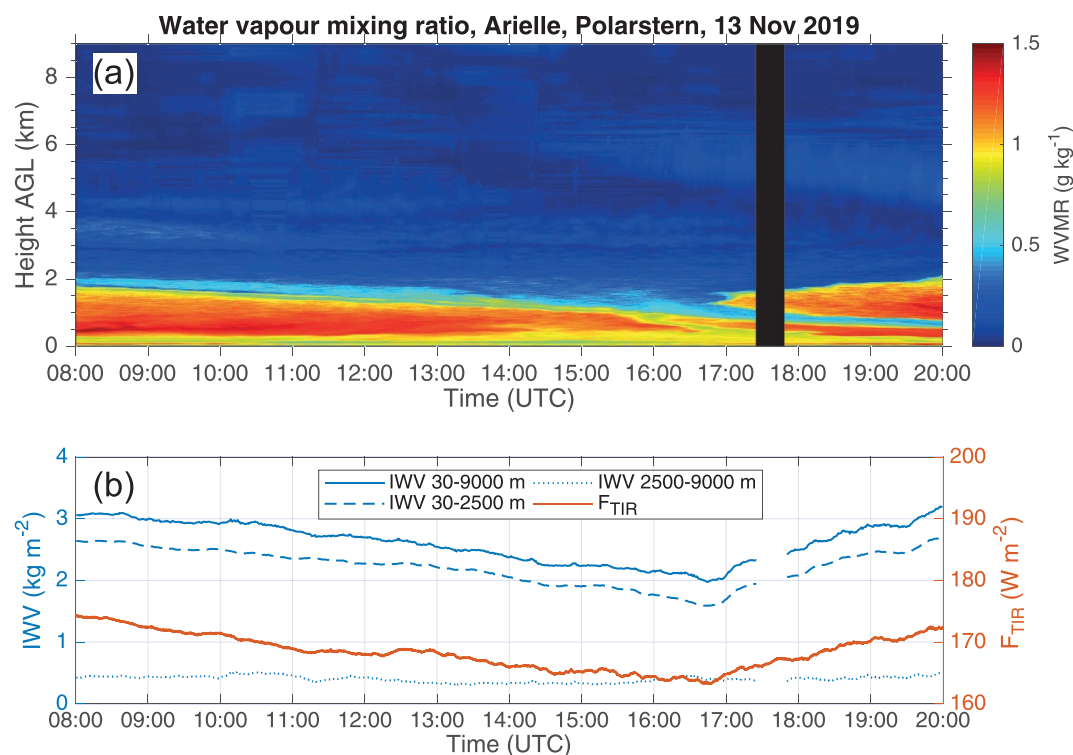


Figure 3. (a) Temporal evolution of the WVMR height distribution measured with a Raman lidar on 13 November 2019 between 08:00 and 20:00 UTC. (b) IWV from the lidar for the height ranges 30–9000 m, 30–2500 m, and 2500–9000 m (Equation 3), and F_{TIR} at the surface.

Figure 3a depicts the temporal development of the height-resolved WVMR distribution for that time period. There are no WVMR measurements for the period between 17:25 UTC and 17:50 UTC due to the regular calibration of the aerosol backscatter channels of the Raman lidar system. The larger WVMR values between ~200 m and ~1,800 m height at 08:00 UTC decrease in height and amount until ~16:44 UTC when a warm and moist air mass is advected to *Polarstern*. This new air mass is sliding on top of the existing colder air mass and replaces it in the course of the day. The moisture arrives in around 1.4 km height and extends in height. After the shown period, a cloud developed between 1,800 and 2,000 m height. Although the WVMR in upper heights results from longer averaging, low values of the WVMR and their changes with time are visible at the upper heights, too.

Using Equation 3, the IWV was calculated from the lidar profiles for the time period on 13 November 2019. The comparison of the lidar-retrieved IWV with the radiosonde-retrieved IWV showed a high concordance with values of 2.77 kg m^{-2} for the lidar and 2.79 kg m^{-2} for the radiosonde at 10:55 UTC and IWV values of 2.01 kg m^{-2} for the lidar and 2.02 kg m^{-2} for the radiosonde at 16:55 UTC. In comparison, the IWV values determined from LHUMPRO showed slightly larger values of 2.90 kg m^{-2} and 2.05 kg m^{-2} as averages from 10:50 UTC to 11:00 UTC and from 16:45 UTC to 16:55 UTC, respectively.

Figure 3b shows the temporal evolution of the lidar-derived IWV for different height ranges together with the measured F_{TIR} at the surface. The result indicates that the IWV changed mainly in heights below 2.5 km on 13 November 2019. There is an almost constant contribution of $\sim 0.4 \text{ kg m}^{-2}$ to the IWV from heights above 2.5 km. F_{TIR} at the surface is linearly correlated with the total IWV as indicated with a coefficient of determination of 0.93 for the period from 08:00 UTC to 16:44 UTC and a coefficient of determination of 0.99 for the period from 16:44 UTC to 20:00 UTC (Figure 4).

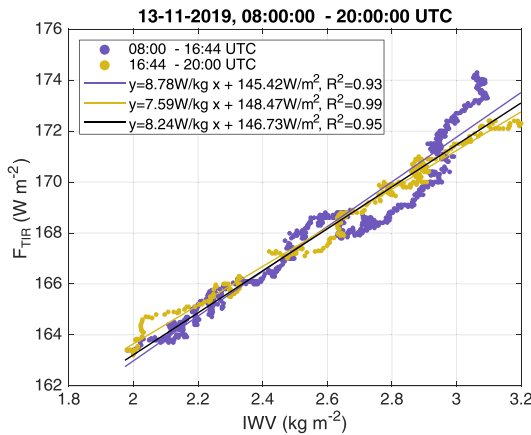


Figure 4. Correlation of the IWV between 30 m height and the tropopause with the F_{TIR} for the descending layer (purple, before 16:44 UTC) and the advected new layer (brown yellow, after 16:44 UTC).

3.2. Relationship of IWV and F_{TIR} for the Slow Transformation of Air Masses

3.2.1. Overview Over Seven Investigated Periods

Six other long-lasting measurements are investigated beside the case on 13 November 2019. The correlation between IWV and F_{TIR} during the seven periods is shown in Figure 5. A clear relationship between IWV and F_{TIR} is found in all seven cases. Details of the analysis to the seven cases are listed in Table 1.

The seven cases in Table 1 differ regarding their representative temperatures T_{rep} and can be divided into three groups:

1. $T_{rep} < -25^{\circ}\text{C}$: cases 6 and 5,
2. $-25^{\circ}\text{C} < T_{rep} < -20^{\circ}\text{C}$: cases 2 and 7,
3. $T_{rep} > -20^{\circ}\text{C}$: cases 4, 3, and 1.

The large coefficients of determination of ≥ 0.8 (in six out of the seven cases) clearly indicate that F_{TIR} is linearly correlated to the IWV for the selected cases with slowly changing air masses. The comparison of the linear correlations shows slight differences in the slope and shifts in the absolute values of F_{TIR} , indicated by different ordinate intercepts of the linear fit equations. It can also be seen from the table that the ordinate intercept tends to be smaller for larger slopes. The different slopes are caused by different IWV values. An additional 1 kg m^{-2} IWV in the atmosphere causes a $7.17 - 12.95\text{ W m}^{-2}$ larger longwave radiation at the surface during cloud-free conditions in the Central Arctic winter. The correlation on 11 December 2019 (case 4) shows with 0.77 a relatively low coefficient of determination due to the small variability both in IWV and F_{TIR} for several hours. On this day, most of the IWV values are between 2.5 kg m^{-2} and 2.8 kg m^{-2} . A rather stable stratification of the atmosphere prevailed on this day.

3.2.2. Impact of Temperature

The impact of the representative temperature of the water vapor profile T_{rep} (cf. Section 2.5) on the relationship between IWV and F_{TIR} is depicted as colors in Figure 5. As can be seen, the same amount of IWV causes a higher downward, broadband thermal-infrared irradiance at the surface, if the temperature of the distributed water vapor is higher. Hence, differences in the atmospheric temperature and water vapor profiles between the cases give an explanation for the shift in the radiation. Larger ordinate intercepts are calculated for cases with higher representative temperatures (cf. Table 1).

In Figures 6 and 7, the temperature T_{rad} (Equation 5) is related to the representative temperature T_{rep} of the vertical distributed water vapor (Equation 7) that emits thermal-infrared radiation. Applying a linear correlation to all data in Figure 6 leads to a coefficient of determination of 0.92. Although already 0.92 shows a high correlation, some reasons are noted in the following to explain deviations from the linear fit. There are further components in the atmosphere emitting thermal-infrared radiation, as for example, molecules (N_2 or O_2), greenhouse gases, haze, and ice crystals in cirrus clouds (Hogan & Bozzo, 2018). All these radiation emitters have different temperatures and will contribute to the resulting F_{TIR} . It has to be noted that the selection of cloud-free measurements is made with the help of the lidar measurements as they easily show clouds. But this selection could only be done for the lidar-observed volume. The lidar has a very narrow vertical-pointing FOV, whereas the pygeometer measures the radiation from the hemisphere. Hence, it cannot be excluded that F_{TIR} measurements are biased by some clouds. But it can also be noted that any (if existing) bias to F_{TIR} did not mask the observed relations. The ordinate intercept of the linear fit is below zero, leading to the conclusion that using the representative temperature of the WVMR profile alone would overestimate the temperature T_{rad} determined from surface radiation measurements.

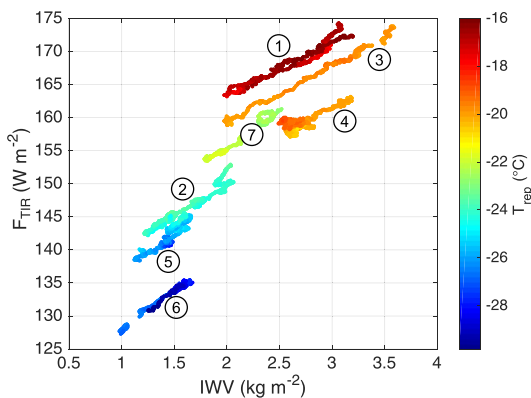


Figure 5. The measured F_{TIR} versus the lidar-derived IWV for the seven selected cloud-free cases. The colors indicate the representative temperature of the water vapor profiles.

Table 1
Seven Cloud-Free Cases Selected for the Analysis of F_{TIR} Correlation With IWV

| Date | Time period [UTC] | Tropopause height [m] | Coeff. of determ. | Slope m [$W\ kg^{-1}$] | Ordinate intercept n [$W\ m^{-2}$] | Repr. temp. T_{rep} [$^{\circ}C$] |
|---------------------------|--------------------------|-----------------------|-------------------|----------------------------|--|---------------------------------------|
| 1 13 November 2019 | 08–20:00 | 9,000 | 0.95 | 8.24 | 146.73 | −16.8 |
| 2 01 and 02 December 2019 | 23:30–10:00 | 8,800 | 0.97 | 9.46 | 130.98 | −24.0 |
| 3 10 December 2019 | 11–16:30 | 9,100 | 0.99 | 8.65 | 141.92 | −19.8 |
| 4 11 December 2019 | 03–20:00, excl. 08–09:00 | 9,100 | 0.77 | 7.17 | 139.77 | −19.9 |
| 5 04 February 2020 | 08–17:30, excl. 11–12:10 | 10,200 | 0.84 | 12.95 | 123.31 | −25.8 |
| 6 11 February 2020 | 02–11:00 | 9,600 | 0.98 | 10.28 | 118.38 | −27.8 |
| 7 23 February 2020 | 16–21:00 | 9,200 | 0.97 | 10.99 | 133.57 | −22.2 |

Note. The slope m and the ordinate intercept n refer to the calculated linear fit equations $y = m \cdot x + n$ of the correlations of each case. The displayed representative temperature depicts the mean of each time period. Note that also aerosol layers were observed during the cases 2–5 (Engelmann et al., 2021).

3.2.3. Impact of the Water Vapor Profile Structures

In Figure 7, the impact of water vapor profile structures on F_{TIR} is illuminated. Therefore, the representative height H_{rep} and the near-surface fraction f_{ns} are used (cf. Section 2.5). The height H_{rep} is the height at which the temperature is equal to the representative temperature T_{rep} . The tendency is for the selected cases that H_{rep} is lower for cases with high T_{rep} and T_{rad} . The temperatures are usually higher at lower altitudes, that is, the water vapor layers at low altitudes are warmer and emit more thermal-infrared radiation than water vapor layers at higher altitudes. That means that larger values of F_{TIR} can often be observed for higher temperatures and larger amounts of water vapor at low altitudes. Because the temperature profiles differ for each of the seven cases, smaller T_{rep} could also be caused by a shift of the whole temperature profile toward lower temperatures. Then, H_{rep} may be lower at smaller T_{rep} than other cases.

For group 1 of the cases (5 and 6) with $T_{rep} < -25^{\circ}C$, we find $H_{rep} > 2500\ m$ (cp. Figure 7a lower left corner). The range of f_{ns} is rather large with values of $0.59 \leq f_{ns} \leq 0.85$ (cp. Figure 7b lower left corner). The IWV is very low for the cases 5 and 6 (cf. Figures 5 and 6). Group 3 of the cases (1, 3, and 4) with $T_{rep} > -20^{\circ}C$ comprises measurements with larger and highly variable IWV values (Figure 6) at high, but less changing T_{rep} . The height H_{rep} shows a rather large range of $1446\ m \leq H_{rep} \leq 2813\ m$ (Figure 7) for those cases. Group 2 of the cases (2 and 7) with $-25^{\circ}C < T_{rep} < -20^{\circ}C$ consists of measurements in between the groups 1 and 3 regarding T_{rep} . The f_{ns} values of $0.61 \leq f_{ns} \leq 0.78$ show a smaller range than group 1 and reach lower minimum values than group 3. The values of H_{rep} lie with $1812\ m \leq H_{rep} \leq 2753\ m$ in the middle of the range of group 3 and mainly below the values of group 1.

The colors in Figures 5 and 7 indicate an impact of T_{rep} , H_{rep} , and f_{ns} on T_{rad} , which implies an impact of the vertical water vapor and temperature distribution on F_{TIR} . The interaction between the different quantities is complex as they are not independent from each other. Especially the near-surface fraction f_{ns} depends on both, the IWV and H_{rep} . Inside slowly changing air masses, the integrated water vapor shows the highest impact on T_{rad} , but also the vertical distribution of water vapor and the temperature profile play a role. Higher temperatures T_{rad} are reached at higher representative temperatures T_{rep} and lower representative heights H_{rep} .

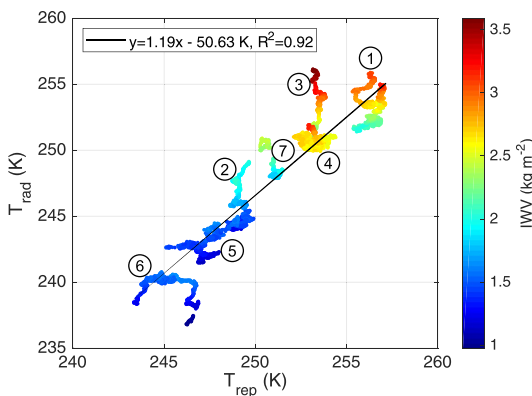


Figure 6. Relationship between the temperature T_{rad} determined from the measured F_{TIR} at the surface (Equation 5), and the representative temperature T_{rep} (Equation 7) of the water vapor profiles for the seven selected cases (Table 1). The total IWV resolved with 10-min resolution is represented by the colors.

3.3. Evaluation of Individual Profiles From Different Air Masses

In the next step, 53 individual WVMR profiles are investigated regarding the relation between IWV and F_{TIR} . The 53 profiles are selected from the whole

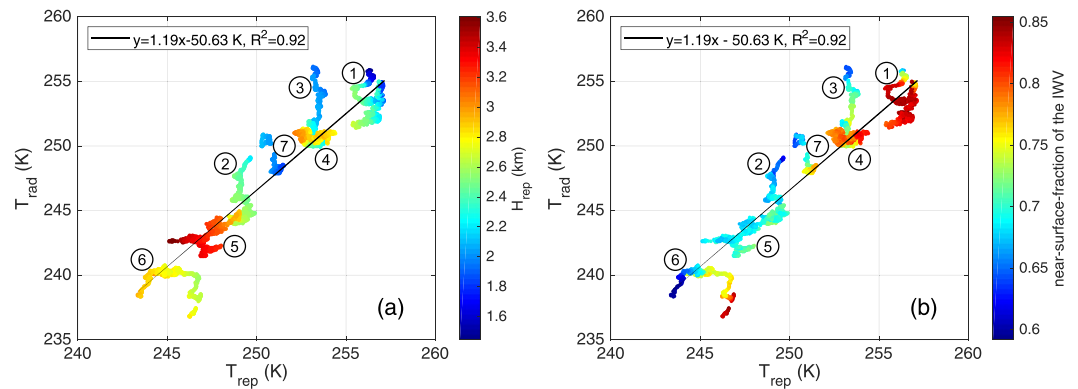


Figure 7. Same as in Figure 6, except that the colors indicate (a) the representative height H_{rep} of the water vapor profile (Section 2.5) and (b) the near-surface fraction of the IWV f_{ns} .

winter period 2019/20 as shown in Figure 2. In contrast to the evaluation of the temporal development of an air mass in Sec. 3.2, these profiles from different days represent independent and varying air masses. Figure 8 shows the relationship of IWV and F_{TIR} for the selected profiles. As expected, low values of F_{TIR} are related to low values of IWV and low representative temperatures T_{rep} , whereas profiles with high IWV values and larger representative temperatures show higher F_{TIR} . The slope of the linear fit between IWV and F_{TIR} for the investigations of the 53 individual measurements is 19.95 W kg^{-1} and the ordinate intercept is 107.22 W m^{-2} , which differs significantly from the coefficients of each of the seven cases of slowly changing air masses (Table 1). However, the slope and the ordinate intercept would be similar if one would fit a linear curve through all the data in Figure 5. Hence, there is no contradiction between the results from the seven slow transformations of air masses and the 53 different air masses. The spread of the data points is mainly related to the temperature impact (see colors in Figure 8). The same total amount of water vapor emits more F_{TIR} at higher temperatures.

Additionally, Figure 8 depicts the domain of the model results from ERA-Interim and JRA-25 reanalyses by Ghatak and Miller (2013) for the winter data. They evaluated monthly mean values from 33 years and found differences between the models, so that the domain of their results is plotted as a gray area here. The results of 53 independent 10-min profiles from measurements fit quite well to the model results; however, they include a large range of values toward low IWV and F_{TIR} values.

In Figures 9 and 10, the temperature T_{rad} is related to the representative temperature T_{rep} of the water vapor profile for the selected profiles. The data points are widely spread around the linear curve. The correlation of T_{rad} with T_{rep} is with 0.71 less than the correlation of the seven cases, shown in Figure 7. The impact of the total IWV

spanning between 0.98 kg m^{-2} and 3.45 kg m^{-2} on the correlation is also evident for the 53 independent 10-min profiles (Figure 9).

Figure 10a shows the same relation between T_{rep} and T_{rad} for the 53 independent 10-min profiles but now with H_{rep} with values between 1,550 m and 3,314 m as the color scale. Figure 10a indicates that the largest H_{rep} are determined for low values of T_{rep} and T_{rad} , whereas H_{rep} is rather small for larger T_{rep} and T_{rad} . In other words, the water vapor is more likely to be found at lower altitudes (smaller H_{rep}) leading to larger T_{rep} and T_{rad} and vice versa. Figure 10b finally displays the same data but using f_{ns} with values between 0.59 and 0.85 as the color scale. A clear impact of f_{ns} is not found. The cases with larger f_{ns} are below the linear fit line. This indicates that additionally to T_{rep} , f_{ns} might have an impact on the intercept with the y-axis.

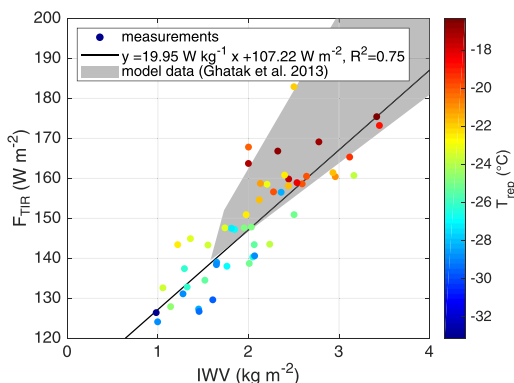


Figure 8. The measured F_{TIR} versus the lidar-derived IWV for 53 selected cloud-free profiles of the winter period 2019/20. The colors represent the representative temperature T_{rep} of the water vapor profiles. The gray area indicates the range of the domain of the model results from ERA-Interim and JRA-25 reanalyses (Ghatak & Miller, 2013).

4. Summary and Conclusion

The impact of the tropospheric water vapor profile on the cloud-free downward, broadband thermal-infrared irradiance at the ground in the Arctic was

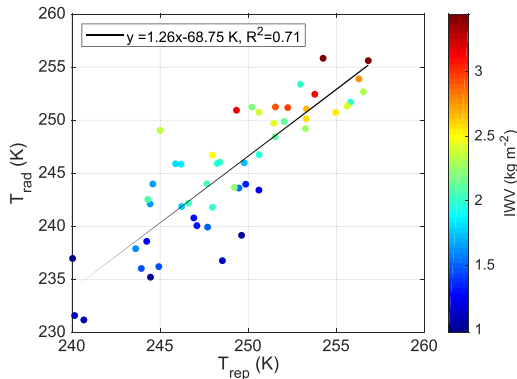


Figure 9. The temperature T_{rad} determined from the measured F_{TIR} at the surface, and the representative temperature T_{rep} of the water vapor profile for the 53 cases. The colors indicate the lidar-derived IWV.

investigated by using measurements north of 85°N during polar night. Raman lidar measurements provided the water vapor information with a high vertical and temporal resolution. Measurements of the lidar backscatter profiles were used to identify cloud-free cases. In general, these data revealed low total integrated water vapor contents with maximum values of 3.6 kg m^{-2} .

The investigation of cloud-free cases was carried out in two ways. Firstly, seven long-lasting cases of slowly changing air masses were examined. Secondly, 53 independent 10-min measurements were studied. The representative temperature T_{rep} of the water vapor distribution (weighted mean temperature) had been defined to characterize the temperature of the radiatively relevant water vapor profile. The height H_{rep} of the representative temperature allowed the definition of the near-surface fraction of the integrated water vapor f_{ns} .

The analysis of the temporal evolution of air masses revealed a linear correlation between F_{TIR} and IWV with coefficients of determination ≥ 0.95 for

five out of seven cases. The slopes and the ordinate intercepts differed for each case and showed a dependence on T_{rep} . The IWV at higher representative temperatures was related to a higher F_{TIR} .

The slope of the linear relations between IWV and F_{TIR} had values between 7.17 and 12.95 W kg^{-1} for the seven long-term observations. These values are higher by about a factor of 2 than respective results obtained from observations at Eureka 80°N (Doyle et al., 2011). This difference goes hand in hand with much larger IWV values of the intrusions investigated by Doyle et al. (2011). The intrusions reflected higher values of the IWV with an average of 5.2 kg m^{-2} , which is larger than the IWV values observed during the MOSAiC wintertime ($\leq 3.6 \text{ kg m}^{-2}$). This also coincides with our results (Table 1 and Figure 5). We obtained larger slopes at lower IWV values.

Heinemann et al. (2022) investigated the relationship between F_{TIR} and the mean specific humidity below 2000 m based on regional climate models with the MOSAiC data as input. They found a linear correlation between F_{TIR} and mean specific humidity for the clear-sky winter data similar to our measurement results. However, Heinemann et al. (2022) revealed a nonlinear relationship between F_{TIR} and mean specific humidity for all-sky conditions.

Additionally, the temperature T_{rad} was determined from F_{TIR} by using the Stefan-Boltzman's law and correlated to T_{rep} with a coefficient of determination of 0.8 for the seven long-term observations. The IWV as well as H_{rep} showed an impact on the relation between the representative temperature of the water vapor profile T_{rep} and the temperature T_{rad} . T_{rep} was usually larger at lower altitudes (H_{rep} smaller) causing larger T_{rad} as well as the integrated water vapor (IWV) was usually larger at higher T_{rep} .

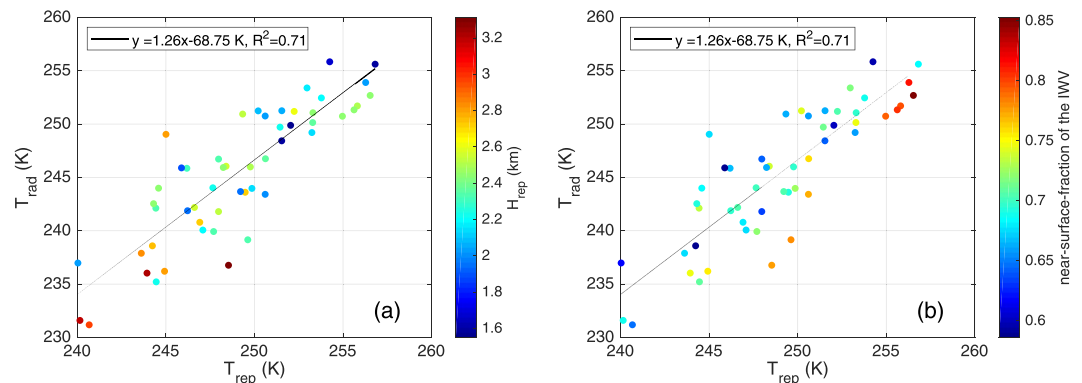


Figure 10. Same as Figure 9, except that the colors indicate (a) the representative height H_{rep} of the water vapor profile and (b) the near-surface fraction of the IWV f_{ns} .

The investigated 53 10-min water vapor profile measurements reflect independent observations of different air masses. The result showed a linear correlation between IWV and F_{TIR} with a dependence of T_{rep} , similar to the evaluation of the temporal development of slowly changing air masses. The applied linear correlation delivered a slope of 19.95 W kg^{-1} and an ordinate intercept of 107.22 W m^{-2} . The relationship between F_{TIR} and the integrated or precipitable water vapor was also studied by Ghatak and Miller (2013). In contrast to our investigations, they used monthly mean values over 33 years from two different models and for all-sky conditions. Their result was a nonlinear relation between the two quantities for all seasons. The data points from the evaluated 53 cloud-free profiles of one winter season in this study fit well with the monthly mean values over several years (Ghatak & Miller, 2013), although different temporal scales of the data are used and the evaluations of cloud-free winter data in this paper cover only a small part of that relation. In contrast to the nonlinear relationship given in the literature for all seasons and all-sky conditions, the relationship between IWV and F_{TIR} was linear for the evaluated cloud-free winter data (coefficient of determination 0.75) with a spread due to different temperatures and other possible influences. Thus, our measurement evaluations reveal that a linear correlation can be used as a first approximation for the relationship between IWV and F_{TIR} for IWV values $\leq 3.6 \text{ kg m}^{-2}$. The temperature T_{rad} was correlated to the representative temperature of the water vapor profile T_{rep} with a coefficient of determination of 0.71. The influence of H_{rep} and f_{ns} was less pronounced due to the large scatter of the data points of the evaluated 53 cloud-free profiles during the winter period of MOSAiC.

The evaluations of our profile measurements show a clear influence of the temperatures of the water vapor along its profile on the F_{TIR} . The profile measurements have a great potential for further evaluations of physical processes in the Arctic atmosphere, and especially as input into models or radiative transfer simulation.

Data Availability Statement

The used data are accessible via the PANGAEA data base. Especially, the radiosonde data are obtainable via Maturilli et al. (2021), the microwave radiometer data (LHUMPRO) are provided via Walbröl, Orlandi, et al. (2022), the profiles of the water vapor mixing ratio measured by the lidar are gainable via Engelmann et al. (2023), and the downward, broadband thermal-infrared irradiance data are receivable via Engelmann et al. (2024).

References

- Barrientos-Velasco, C., Deneke, H., Hünerbein, A., Griesche, H. J., Seifert, P., & Macke, A. (2022). Radiative closure and cloud effects on the radiation budget based on satellite and shipborne observations during the arctic summer research cruise, ps106. *Atmospheric Chemistry and Physics*, 22(14), 9313–9348. <https://doi.org/10.5194/acp-2021-1004>
- Boeke, R. C., & Taylor, P. C. (2018). Seasonal energy exchange in sea ice retreat regions contributes to differences in projected Arctic warming. *Nature Communications*, 9(1), 1–14. <https://doi.org/10.1038/s41467-018-07061-9>
- Bozem, H., Hoor, P., Kunkel, D., Köllner, F., Schneider, J., Herber, A., et al. (2019). Characterization of transport regimes and the polar dome during arctic spring and summer using in situ aircraft measurements. *Atmospheric Chemistry and Physics*, 19(23), 15049–15071. <https://doi.org/10.5194/acp-19-15049-2019>
- Clark, J., Clothiaux, E., Feldstein, S., & Lee, S. (2021). Drivers of global clear sky surface downwelling longwave irradiance trends from 1984 to 2017. *Geophysical Research Letters*, 48(22), e2021GL093961. <https://doi.org/10.1029/2021GL093961>
- Dai, G., Althausen, D., Hofer, J., Engelmann, R., Seifert, P., Bühl, J., et al. (2018). Calibration of Raman lidar water vapor profiles by means of AERONET photometer observations and GDAS meteorological data. *Atmospheric Measurement Techniques*, 11(5), 2735–2748. <https://doi.org/10.5194/amt-11-2735-2018>
- Doyle, J. G., Lesins, G., Thackray, C. P., Perro, C., Nott, G. J., Duck, T. J., et al. (2011). Water vapor intrusions into the high Arctic during winter. *Geophysical Research Letters*, 38(12). <https://doi.org/10.1029/2011GL047493>
- Elgered, G., Rönnäng, B., & Askne, J. (1982). Measurements of atmospheric water vapor with microwave radiometry. *Radio Science*, 17(5), 1258–1264. <https://doi.org/10.1029/RS017i005p01258>
- Engelmann, R., Ansmann, A., Ohneiser, K., Griesche, H., Radenz, M., Hofer, J., et al. (2021). Wildfire smoke, Arctic haze, and aerosol effects on mixed-phase and cirrus clouds over the North Pole region during MOSAiC: An introduction. *Atmospheric Chemistry and Physics*, 21(17), 13397–13423. <https://doi.org/10.5194/acp-21-13397-2021>
- Engelmann, R., Griesche, H., Radenz, M., Hofer, J., Althausen, D., Hengst, R., & Barrientos Velasco, C. (2024). Continuous radiation measurements during the POLARSTERN cruise PS122/1-5, 06 October 2019–02 October 2020, Arctic Ocean [Dataset]. PANGAEA. <https://doi.org/10.1594/PANGAEA.968751>
- Engelmann, R., Griesche, H., Radenz, M., Hofer, J., Althausen, D., Seidel, C., et al. (2023). Water vapor profiles retrieved during the polarstern cruises ps122/1, ps122/2 and ps122/3, 28 september 2019–29 february 2020, Arctic Ocean. <https://doi.org/10.1594/PANGAEA.957158>
- Engelmann, R., Kanitz, T., Baars, H., Heese, B., Althausen, D., Skupin, A., et al. (2016). The automated multiwavelength Raman polarization and water-vapor lidar PollyXT: The neXT generation. *Atmospheric Measurement Techniques*, 9(4), 1767–1784. <https://doi.org/10.5194/amt-9-1767-2016>
- Foth, A., Baars, H., Di Girolamo, P., & Pospichal, B. (2015). Water vapour profiles from Raman lidar automatically calibrated by microwave radiometer data during HOPE. *Atmospheric Chemistry and Physics*, 15(14), 7753–7763. <https://doi.org/10.5194/acp-15-7753-2015>

Acknowledgments

Data used in this article were produced as part of the international Multidisciplinary drifting Observatory for the Study of the Arctic Climate (MOSAIC) with the tag MOSAiC20192020 and the Project_ID: AWI_PS122_00. We would like to thank everyone who contributed to the measurements used here (Nixdorf et al., 2021). Radiosonde data were obtained through a partnership between the leading Alfred Wegener Institute, the Atmospheric Radiation Measurement user facility, a U.S. Department of Energy facility managed by the Biological and Environmental Research Program, and the German Weather Service (DWD). We would like to thank the RV Polarstern crew for their perfect logistical support during the 1-year MOSAiC expedition. This project has also received funding from ACTRIS-D. ACTRIS-D is funded by the German Federal Ministry for Education and Research (BMBF) under grant agreements 01LK2001A-K and 01LK2002A-G. We also acknowledge the funding by the Deutsche Forschungsgemeinschaft (DFG, German Research Foundation)—Project-ID 268020496—TRR 172. Open Access funding enabled and organized by Projekt DEAL.

- Ghatak, D., & Miller, J. (2013). Implications for Arctic amplification of changes in the strength of the water vapor feedback. *Journal of Geophysical Research: Atmospheres*, *118*(14), 7569–7578. <https://doi.org/10.1002/jgrd.50578>
- Graversen, R. G., Mauritsen, T., Tjernström, M., Källén, E., & Svensson, G. (2008). Vertical structure of recent Arctic warming. *Nature*, *451*(7174), 53–56. <https://doi.org/10.1038/nature06502>
- Heese, B., Flentje, H., Althausen, D., Ansmann, A., & Frey, S. (2010). Ceilometer lidar comparison: Backscatter coefficient retrieval and signal-to-noise ratio determination. *Atmospheric Measurement Techniques*, *3*(6), 1763–1770. <https://doi.org/10.5194/amt-3-1763-2010>
- Heinemann, G., Schefczyk, L., Willmes, S., & Shupe, M. D. (2022). Evaluation of simulations of near-surface variables using the regional climate model CCLM for the mosaic winter period. *Elementa*, *10*(1). <https://doi.org/10.1525/elementa.2022.00033>
- Hogan, R. J., & Bozzo, A. (2018). A flexible and efficient radiation scheme for the ecmwf model. *Journal of Advances in Modeling Earth Systems*, *10*(8), 1990–2008. <https://doi.org/10.1029/2018MS001364>
- Jin, X., Barber, D., & Papakyriakou, T. (2006). A new clear-sky downward longwave radiative flux parameterization for arctic areas based on rawinsonde data. *Journal of Geophysical Research*, *111*(D24). <https://doi.org/10.1029/2005JD007039>
- Knust, R. (2017). Polar research and supply vessel polarstern operated by the alfred-wegener-institute. *Journal of Large-Scale Research Facilities JLSRF*, *3*, A119. <https://doi.org/10.17815/jlsrf-3-163>
- Law, K. S., Stohl, A., Quinn, P. K., Brock, C. A., Burkhardt, J. F., Paris, J.-D., et al. (2014). Arctic air pollution: New insights from polarcat-ipy. *Bulletin of the American Meteorological Society*, *95*(12), 1873–1895. <https://doi.org/10.1175/BAMS-D-13-00017.1>
- Maturilli, M., Holdridge, D. J., Dahlke, S., Graeser, J., Sommerfeld, A., Jaiser, R., et al. (2021). Initial radiosonde data from 2019–10 to 2020–09 during project MOSAiC [Dataset]. PANGAEA. <https://doi.org/10.1594/PANGAEA.928656>
- Melfi, S., Lawrence Jr, J., & McCormick, M. (1969). Observation of Raman scattering by water vapor in the atmosphere. *Applied Physics Letters*, *15*(9), 295–297. <https://doi.org/10.1063/1.1653005>
- Melfi, S., & Whiteman, D. (1985). Observation of lower-atmospheric moisture structure and its evolution using a Raman lidar. *Bulletin of the American Meteorological Society*, *66*(10), 1288–1292. [https://doi.org/10.1175/1520-0477\(1985\)066<1288:OOLAMS>2.0.CO;2](https://doi.org/10.1175/1520-0477(1985)066<1288:OOLAMS>2.0.CO;2)
- Myhre, G., Shindell, D., Bréon, F.-M., Collins, W., Fuglestedt, J., Huang, J., et al. (2013). Anthropogenic and natural radiative forcing [Book Section]. In T. F. Stocker, D. Qin, G.-K. Plattner, M. M. B. Tignor, S. K. Allen, J. Boschung, et al. (Eds.), *Climate change 2013: The Physical Science Basis. Contribution of Working Group I to the Fifth Assessment Report of the Intergovernmental Panel on Climate Change* (pp. 659–740). <https://doi.org/10.1017/CBO9781107415324.018>
- Nash, D., Waliser, D., Guan, B., Ye, H., & Ralph, F. M. (2018). The role of atmospheric rivers in extratropical and polar hydroclimate. *Journal of Geophysical Research: Atmospheres*, *123*(13), 6804–6821. <https://doi.org/10.1029/2017JD028130>
- Nixdorf, U., Dethloff, K., Rex, M., Shupe, M., Sommerfeld, A., Perovich, D. K., et al. (2021). Mosaic extended acknowledgement. *Zenodo*. <https://doi.org/10.5281/zenodo.5541624>
- Ohneiser, K., Ansmann, A., Chudnovsky, A., Engelmann, R., Ritter, C., Veselovskii, I., et al. (2021). The unexpected smoke layer in the high Arctic winter stratosphere during MOSAIC 2019–2020. *Atmospheric Chemistry and Physics*, *21*(20), 15783–15808. <https://doi.org/10.5194/acp-21-15783-2021>
- Pace, G., di Sarra, A., Cali Quaglia, F., Ciardini, V., Di Iorio, T., Iaccarino, A., et al. (2023). Verification of parameterizations for clear sky downwelling longwave irradiance in the Arctic. *Atmospheric Measurement Techniques Discussions*, 1–24. <https://doi.org/10.5194/amt-2023-181>
- Rinke, A., Cassano, J. J., Cassano, E. N., Jaiser, R., & Handorf, D. (2021). Meteorological conditions during the mosaic expedition: Normal or anomalous? *Elementa-Science of the Anthropocene*, *9*(1), 00023. <https://doi.org/10.1525/elementa.2021.00023>
- Ruckstuhl, C., Philipona, R., Morland, J., & Ohmura, A. (2007). Observed relationship between surface specific humidity, integrated water vapor, and longwave downward radiation at different altitudes. *Journal of Geophysical Research*, *112*(D3). <https://doi.org/10.1029/2006JD007850>
- Screen, J. A., & Simmonds, I. (2010). The central role of diminishing sea ice in recent Arctic temperature amplification. *Nature*, *464*(7293), 1334–1337. <https://doi.org/10.1038/nature09051>
- Seidel, C. (2022). *Analysis of water vapour mixing ratio profiles in the arctic from Raman lidar measurements during the mosaic-campaign*. Masterarbeit, University of Leipzig. Retrieved from <https://nbn-resolving.org/urn:nbn:de:bsz:15-qucosa2-845481>
- Shupe, M. D., Rex, M., Blomquist, B., Persson, P. O. G., Schmale, J., Uttal, T., et al. (2022). Overview of the mosaic expedition: Atmosphere. *Elementa: Science of the Anthropocene*, *10*(1). <https://doi.org/10.1525/elementa.2021.00060>
- Survo, P., Turunen, M., Salo, T., & Jauhiainen, H. (2014). *Vaisala radiosonde RS41—new sensing technologies for operational upper air measurements*. TECO-2014, St. Petersburg, Russian Federation.
- Town, M. S., Walden, V. P., & Warren, S. G. (2005). Spectral and broadband longwave downwelling radiative fluxes, cloud radiative forcing, and fractional cloud cover over the south pole. *Journal of Climate*, *18*(20), 4235–4252. <https://doi.org/10.1175/JCLI3525.1>
- Walbröl, A., Crewell, S., Engelmann, R., Orlandi, E., Griesche, H., Radenz, M., et al. (2022). Atmospheric temperature, water vapour and liquid water path from two microwave radiometers during mosaic. *Scientific Data*, *9*(1), 1–15. <https://doi.org/10.1038/s41597-022-01504-1>
- Walbröl, A., Orlandi, E., Crewell, S., & Ebell, K. (2022). Integrated water vapour derived from the mirac-p microwave radiometer onboard the polarstern during the mosaic expedition [Dataset]. PANGAEA. <https://doi.org/10.1594/PANGAEA.941470>
- Wandinger, U. (2005). Raman lidar. In *Lidar—Range-resolved optical remote sensing of the atmosphere* (pp. 241–271). Springer.
- Weitkamp, C. (2006). *Lidar: Range-resolved optical remote sensing of the atmosphere* (Vol. 102). Springer Science & Business.
- Wendisch, M., Brückner, M., Burrows, J., Crewell, S., Dethloff, K., Ebell, K., et al. (2017). Understanding causes and effects of rapid warming in the Arctic. *Eos*, *98*. <https://doi.org/10.1029/2017eo064803>
- Wendisch, M., Brückner, M., Crewell, S., Ehrlich, A., Notholt, J., Lüpkes, C., et al. (2023). Atmospheric and surface processes, and feedback mechanisms determining arctic amplification: A review of first results and prospects of the (ac)² project. *Bulletin of the American Meteorological Society*, *104*(1), E208–E242. <https://doi.org/10.1175/BAMS-D-21-0218.1>
- Whiteman, D. N. (2003a). Examination of the traditional Raman lidar technique. I. Evaluating the temperature-dependent lidar equations. *Applied Optics*, *42*(15), 2571–2592. <https://doi.org/10.1364/AO.42.002571>
- Whiteman, D. N. (2003b). Examination of the traditional Raman lidar technique. II. Evaluating the ratios for water vapor and aerosols. *Applied Optics*, *42*(15), 2593–2608. <https://doi.org/10.1364/AO.42.002593>